

Half-metallicity and wandering axis ferromagnetism in Mn substituted Fe₂TiSn

Kulbhusan Mishra,¹ Shishir Kumar Pandey,² S. Chaudhuri,³ Rajiv Rawat,⁴ and P. A. Bhobe^{1,*}

¹Indian Institute of Technology, Khandwa Road, Indore, Simrol, 453552, India

²Birla Institute of Technology & Science, Pilani Dubai Campus,

Dubai International Academic City, P.O. Box No. - 345055, Dubai, UAE

³Center for Condensed Matter Science, National Taiwan University, Taipei 10617 Taiwan

⁴UGC-DAE Consortium for Scientific Research, University Campus, Khandwa Road, Indore 452001, India

(Dated: July 17, 2024)

We investigate the effect of Mn substitution in Fe₂Ti_{1-x}Mn_xSn on electronic structure, magnetic and electrical transport properties. The spin-polarized density of states calculations using density-functional theory (DFT), yields a half-metallic ground state in Mn-rich compositions. Localized magnetic moments at Mn sites that interact through the cloud of conduction electrons formed by Fe and Ti atoms are also predicted. Electrical resistivity and magneto-transport measurements reveal a Kondo-like ground state at low temperatures and a peculiar linear negative temperature coefficient of resistance in the high-temperature regime with a predominant electron-phonon scattering mechanism. Analysis of room temperature powder X-ray diffraction data reveals a highly ordered L₂₁ structure and reduction of antisite disorder, upon Mn substitution. The temperature-dependent magnetization measurements reveal distinct features indicative of weak anisotropy in the system. Isothermal magnetization measured as a function of the applied field helps identify the unique magnetic ground state of the half-metallic Fe₂Ti_{1-x}Mn_xSn composition as a ferromagnet with a wandering axis, that distinctively orients in the direction of applied field. Our findings thus provide a new perspective for studying the mechanism of half-metallicity and associated magnetic order in Heuslers.

I. INTRODUCTION

Since its discovery in 1903[1], Heusler alloys with general formula X₂YZ (where X and Y are transition metals and Z is the main group element), have constantly drawn attention of the researchers due to its remarkable properties, such as magnetic shape memory effect[2], near - room temperature magnetocaloric effect[3], half-metallic ferromagnetism[4, 5], spin-gapless semi-conductivity, unconventional superconductivity[6] and anomalous Hall effect, and so on. These compositions crystallize in the L₂₁ structure (space group: *Fm-3m*) consisting of 4 interpenetrating FCC sublattices, where X atom occupies the (0.25,0.25,0.25) and (0.75,0.75,0.75) sublattice sites, whereas the Y and Z atoms occupy the (0.5,0.5,0.5) and (0,0,0) sublattice sites, respectively. Theoretical studies on Heusler alloys reveal an interesting relationship between the total spin moment per unit cell (M_T) and the number of valence electrons count (VEC) per formula unit (Z). Also known as Slater-Pauling rule[7], this relationship states quantitative value of M_T as equal to (Z - 24), and seems to provide a handle to modulate the physical properties of Heuslers through suitable chemical substitutions.

Ideally, for compositions where VEC equals 24, the Slater-Pauling rule suggests a non-magnetic ground state. Examples include the Fe₂VAl, Fe₂VGa[8, 9] compositions. However, experimental studies of the magnetic properties show signatures of weak magnetism[10, 11], the reason being presence of anti-site and quenched

disorders[12]. Heusler alloys with VEC 24 are also considered for applications such as magnetic information storage where they could play the role of a thin non-magnetic buffer layer sandwiched between two ferromagnetic layers of other Heusler compositions, acting as a spin polarizer in a recording head while providing the very compatible inter-layer coupling. Furthermore, a significant decrease in the resistivity, magnetization, and magnetoresistance values has been reported. When other transition metal atom are substituted at X or Y sites, that can lead to a state of high spin-polarization[13] at Fermi level. A narrow gap/ pseudogap forms in the vicinity of the Fermi level with transport measurements reflecting a semiconducting nature and heavy effective mass of charge carriers. These properties make them suitable for thermoelectric applications.

Another notable example is the Fe₂TiSn composition, which conforms to the VEC = 24 prototype. The electronic structure calculation indicates Fe₂TiSn to be a non-magnetic semimetal with a pseudogap in the density of state at Fermi level. Based on specific heat measurements, it has been speculated to be a heavy fermion metal with quasi-particle mass $\sim 40 m_e$ [14]. The substitution of Ni at Fe sites forms a system with isolated spins leading to a Kondo-like interaction between localized spins and conduction electrons [15]. On the contrary, Co substitution leads to a typical spin fluctuation scenario. Optical conductivity and infrared studies provide evidence of pseudogap in the density of states and, the mass enhancement at low temperature to be Schottky anomaly from magnetic clusters resulting from antisite disorder between Fe and Ti sites. In contrast, Sayan et al. have shown that the substitution of a small percentage of Ti at the Fe site reduces antisite disorder and resistivity

* pbhobe@iiti.ac.in

and specific heat measurements suggest the presence of spin fluctuation, which decreases with decreasing disorder. It is to be noted here that in contrast to Fe and Co, bulk Ni has a sharp peak at E_f in one of the spin subbands[16]. This sudden increase of DOS at E_f may lead to enhanced electron-electron interaction (EEI) leading to Kondo-like spin scattering at low temperature. Furthermore, the non-magnetic semi-metallic band structure of Fe_2TiSn demonstrates a low density of states at the Fermi level, rendering the electronic structure and magnetic properties highly sensitive to doping or elemental substitution and with proper substitution at Ti and Sn sites, the system can be driven to half-metallicity[17, 18].

In this work, we report the detailed investigation of the structural, magnetic, and transport properties of Mn-substituted Fe_2TiSn compositions. X-ray diffraction (XRD) results show the formation of an ordered L_{21} structure with highly reduced antisite disorder. Temperature and field-dependent magnetization measurements indicate the presence of anisotropy in the system, due to the strong local magnetic moment of Mn atoms. The low-temperature upturn in the electrical resistivity is due to the combined effect of electron-electron correlation and strong Kondo-like spin scattering. The $\rho(T)$ above 100 K can be best explained by electron-phonon and electron-magnon scattering, and the contribution of electron-magnon scattering is comparatively less, which indicates the presence of spin polarization of density of state in the prepared composition. We have also performed the electronic structure calculations to better understand the ground state properties.

II. EXPERIMENTAL AND COMPUTATIONAL DETAILS

Polycrystalline $\text{Fe}_2\text{Ti}_{1-x}\text{Mn}_x\text{Sn}$ compositions were prepared by melting stoichiometric amounts of high purity (99.99%) elements such as, Fe, Mn, Ti, and Sn using an electric arc furnace by placing these elements on a water-cooled Cu hearth and under flowing Ar atmosphere. The homogeneous ingots thus formed were vacuum sealed in the quartz tubes and annealed for 72 hours at 800°C followed by quenching in ice water. The weight loss during the whole process was $\leq 1\%$. The energy dispersive X-ray spectroscopy (EDS), equipped with a field emission scanning electron microscope was performed using Model FE-SEM Supra 55 (Carl Zeiss, Germany), to ensure the target composition after melting was close to the starting stoichiometry. The atomic percentages of the elements are presented in Table I and the elemental mapping for $x = 0.25$ is shown in Fig.1. The crystallographic phase purity of the samples checked using a laboratory X-ray source, on Bruker D8 Advance diffractometer having Cu target ($\lambda = 1.5406 \text{ \AA}$), confirms the formation of the Heusler phase. Magnetization as a function of temperature and magnetic field is measured using a Quantum Design SQUID magnetometer. A standard four-probe

method with a homemade resistivity setup equipped with a superconducting magnet system was used for the electrical resistivity and magnetoresistance measurements.

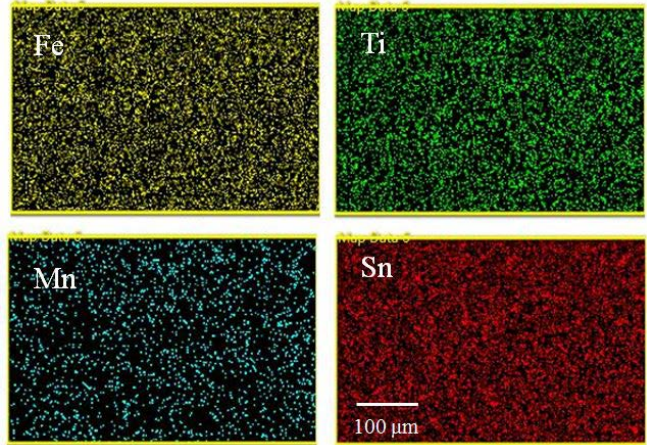


FIG. 1. The elemental mapping results of $x = 0.25$. The figures are presented at a scale of $100 \mu\text{m}$.

Density-functional theory (DFT) calculations are performed within the Quantum Espresso package [19, 20] where ultrasoft pseudopotentials [21] and a plane-wave basis set are employed. Generalized-gradient approximation (GGA) with Perdew–Burke–Ernzerhof (PBE) functional form is used for the calculation of exchange-correlation energy [22]. For Sn, Ti, Mn and Fe, $4d^{10}5s^25p^1$, $3s^23p^64s^23d^1$, $s^23p^64s^{1.5}3d^54p^0$ and $3s^24s^23p^63d^6$ are treated as valence states respectively. The kinetic energy cutoff for plane-wave functions of 95 Ry and the charge density of 1140 Ry are considered in our calculations. We start with the simple cubic crystal structure (space group: $Fm - 3m$, no: 225) of Fe_2TiSn with lattice constant $a = 6.059 \text{ \AA}$ and fully optimize it after replacing one of the Ti atoms with Mn (25 % doping). Energy convergence criterion of 5×10^{-7} Ry and $6 \times 6 \times 6$ uniform k -mesh and Marzari-Vanderbilt smearing are considered in our calculations. The optimization leads to small changes ($< 1.0 \%$) in the lattice constants. These spin-polarized calculations are performed starting with aligning all eight Fe atoms ferromagnetically with large moments while the one Mn atom is aligned anti-ferromagnetically to the Fe atoms in the total 16-atom unit cell. However, after the convergence, the negligibly small Fe and large Mn magnetic moments are aligned ferromagnetically. We discuss these results in connection with the magnetic properties of the compositions, at a later stage.

For the present calculation, the Mn-Mn magnetic interaction is estimated by considering $2 \times 2 \times 2$ supercell of 128 atoms and replacing two Ti atoms with Mn. The different separation between these two Mn atoms within this supercell is then considered to extract the distance-dependent magnetic interaction. The four possible Mn-Mn separations considered, after avoiding the possible in-

TABLE I. Atomic percentages, parameters determining goodness of fit and magnetic transition temperatures of $\text{Fe}_2\text{Ti}_{1-x}\text{Mn}_x\text{Sn}$.

Composition	Atomic %				goodness of fit			T_C (K)	T_S (K)
	Fe	Ti	Mn	Sn	R_{Bragg}	R_F	χ^2		
0.05	48.05	24.51	1.23	26.21	8.12	10.1	1.94	< 5	250
0.10	48.29	22.76	2.55	26.27	8.44	6.49	2.51	6	268
0.25	48.0	19.55	6.25	26.13	9.68	7.86	2.77	18	320
0.30	47.91	18.10	7.40	26.60	10.7	9.09	2.02	25	325

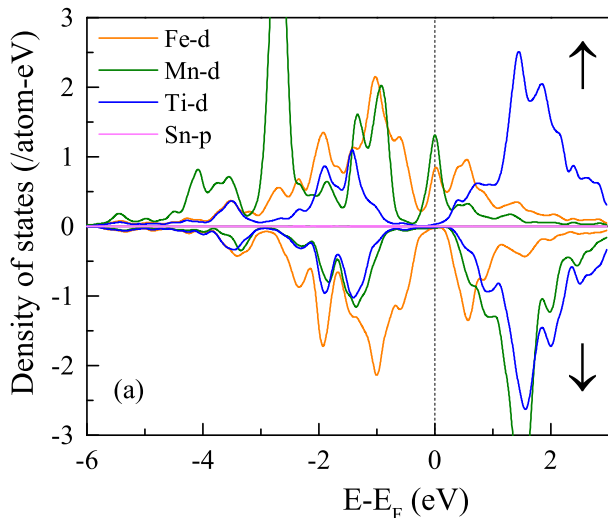


FIG. 2. Atom-projected spin-polarized density of states for Fe, Mn, and Ti $-d$ and Sn p orbitals in $\text{Fe}_2\text{Ti}_{0.75}\text{Mn}_{0.25}\text{Sn}$ in the ferromagnetic arrangements. Contributions from both Fe and Mn d states in the up spin channel at the Fermi level (set to zero) signify the itinerant magnetic interaction between these two atoms. Contributions from Ti d and Sn p orbitals are either below or above the Fermi level.

terference of periodic images of supercell on magnetic interactions, are 4.254, 6.017, 7.369, and 8.509 Å. At these four distances, magnetic interaction is estimated by calculating the energy difference between ferromagnetic and antiferromagnetic arrangements of the two Mn atoms. Background from negligibly small Fe and Ti magnetic moments has an insignificant influence on the magnetic interactions estimated in this fashion.

III. RESULTS AND DISCUSSION

The density of states (DOS) scenario of the $\text{Fe}_2\text{Ti}_{1-x}\text{Mn}_x\text{Sn}$ system is obtained using a DFT-only approach. The atom-projected spin-polarized DOS of Fe, Mn, Ti $-d$ and Sn p states for this case are shown in Fig. 2. Many insightful observations can be made from this plot. First, the system shows the half-metallic character of the DOS with mainly Fe and Mn d states in the spin-up channel, while there is a band gap in the spin-down channel at the Fermi level. Though Ti d states

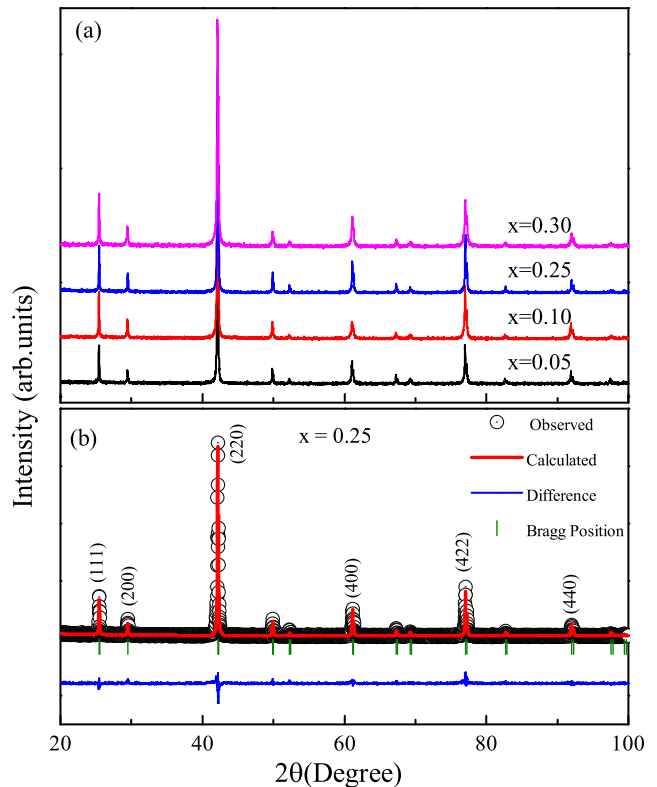


FIG. 3. (a) X-ray diffraction profile of $\text{Fe}_2\text{Ti}_{1-x}\text{Mn}_x\text{Sn}$, and (b) Rietveld refined XRD profile of $x=0.25$.

also contribute below the Fermi level, the dominant contributors remain to be the d states of Fe and Mn atoms, and the magnetic properties arise from the interactions among all three transition metal atoms. Second, this interaction can safely be assumed to be itinerant as the system is metallic. Third, the magnetic moment on the Mn site is large, while Fe and Ti atoms carry negligible moment while both, Mn & Fe have finite contribution to the DOS at the Fermi level. Recall that we started with a scenario of antiferromagnetic coupling between single Mn and eight (ferromagnetically aligned) Fe atoms. Such a system converges to a ferromagnetic coupling among all the magnetic atoms, with negligibly small magnetic moments on Fe ($\sim 0.016 \mu_B$) and Ti ($\sim 0.052 \mu_B$) atoms, and a relatively high moment on Mn ($\sim 3.161 \mu_B$) atoms. It appears as if Mn atoms are the ones with localized

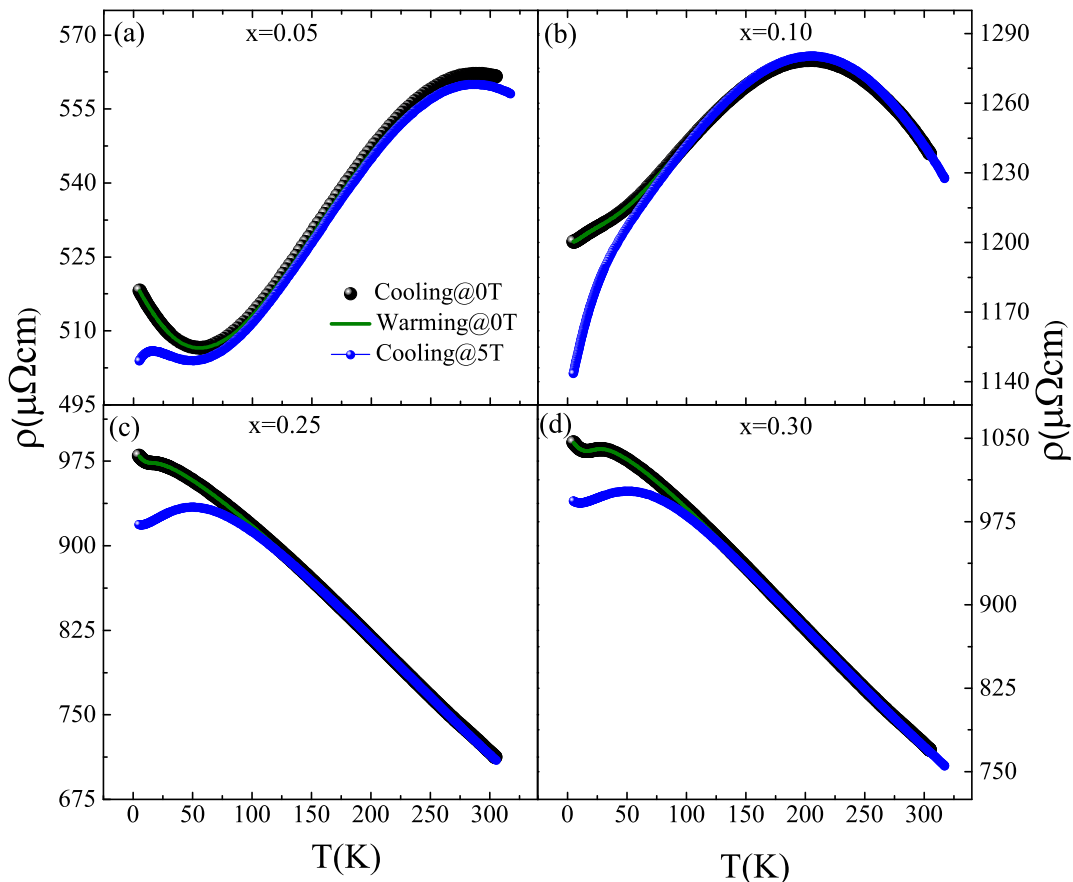


FIG. 4. Temperature dependent resistivity of $\text{Fe}_2\text{Ti}_{1-x}\text{Mn}_x\text{Sn}$ measured at an applied field of 0 and 5 T.

moments that are interacting through the cloud of conduction electrons formed by Fe and Ti atoms.

With the intent of finding a half-metallic Heusler, we begin the experimental investigation into the Mn-substituted Fe_2TiSn compounds. The X-ray diffraction (XRD) patterns of $\text{Fe}_2\text{Ti}_{1-x}\text{Mn}_x\text{Sn}$ ($x = 0.05, 0.1, 0.25,$ and 0.3) are shown in Fig.3(a). The presence of strong (111), (200), and (220) peaks confirm the highly ordered cubic $L2_1$ crystal structure in all the prepared compositions. However, the solubility limit of Mn in Fe_2TiSn is limited to 30% as additional peaks related to the secondary phase begin to appear for compositions with $x \geq 0.4$. Contrary to the general expectation of finding an increase in the antisite disorder upon carrying out substitutions in an intermetallic system, the present compositions show a relative increase in the intensity of the (111) and (200) super-lattice peaks, indicating a reduction of the overall disorder in comparison to pristine Fe_2TiSn . Rietveld refinement of the XRD profiles, implemented through the FullProf suite[23], yield values for lattice parameters that follow Vegard's law[24] indicating the desired substitutions at the targeted lattice sites have indeed been achieved.

With the prediction of half-metallic DOS at the Fermi level and a highly ordered crystal structure, it becomes

pertinent to study the electrical resistivity of the Mn-substituted Fe_2TiSn compounds. Fig.4 presents the $\rho(T)$ measured for all the compositions in the temperature range of 5–320 K and with a constant magnetic field of 0 and 5 T. For low Mn-concentration of $x = 0.05$ and 0.1 , $\rho(T)$ decreases with decreasing temperature, displaying the expected metallic character. However, for the half-metallic composition of $x = 0.25$ (and also for $x = 0.3$), $\rho(T)$ changes dramatically with a negative temperature coefficient of resistance (TCR) in the given temperature range. The overall magnitude of resistivity also increases as x changes from 0.05 to 0.3, while in principle, overall valence electron count increases with the systematic replacement of Ti with Mn takes place. A careful analysis of $\rho(T)$ in the different temperature segments hence becomes necessary to bring to the fore the underlying charge scattering mechanisms.

Firstly, the presence of a narrow gap in one of the spin sub-bands that has its origin in a half-metallic band structure can give rise to an increased magnitude of resistivity due to the absence of the spin-flip level in the electron-magnon scattering process[25–27]. A negative TCR in $x = 0.25$ (and 0.3) is also not an unusual trend in Heuslers and many quaternary and half-Heusler compounds are known to show such dependence[28–30].

However, the interesting aspect here is the near linear $\rho(T)$ between 100 to 300 K, rather than a thermally activated power law or an exponentially decaying function. A good fit to the data in this temperature region is obtained through a combination of the highly dominant electron-phonon scattering process (T linear term) along with a small contribution of electron-magnon scattering (T^2 term), as described by the equation, $\rho(T) = \rho_0 + \rho_{ep}T + \rho_{em}T^2$ and displayed in Fig.5. Since the $e-m$ scattering is a spin-flip process, the whole spin wave needs to consist of both the spin-up and spin-down sub-bands. The significantly low value of ρ_{em} as compared to the ρ_{ep} denotes the absence of one of the spin density of state through opening of the gap at the Fermi level, leading to the formation of the spin-polarized band structure, and agreeing with our electronic structure calculations.

In the same temperature range, the compositions with low Mn concentration of $x = 0.05, 0.1$ display the expected metallic behavior, with its characteristic broad hump-feature. On the high-temperature side of the hump-feature lies the semi-metallic nature of Fe_2TiSn , while the low-temperature side is the typical metallic conduction[31]. The reason for the broad hump-feature itself, is the short-range magnetic clusters that are known to form even in pristine Fe_2TiSn due to the sizable antisite disorder between Fe & Ti atoms, as already shown in literature[17]. In the compositions containing low Mn percentages, the peak of the hump-feature is shifted to a slightly lower temperature. The sizeable effect of antisite disorder is also seen at the low temperature, wherein $\rho(T)$ experiences an upturn for $x = 0.05$ and 0.1 . Recent studies have shown that the application of a constant external magnetic field overcomes this upturn and signifies the presence of weak localization in Fe_2TiSn [17] and the same scenario applies to these low Mn-substituted compositions.

On the other hand for compositions with $x = 0.25, 0.3$, the negative TCR in $\rho(T)$ continues until a cusp-like feature occurs at temperatures below 20 K. This feature gets suppressed upon application of a constant external magnetic field, without any effect on the high-temperature linear resistivity. The data in the low-temperature region does not fit the simple description of weak localization, as was the case for $x = 0.05, 0.1$ compositions. Rather, a good fit to the data below 20 K and for $H = 0$ & 5 T is obtained using the description,

$$\rho(T) = \rho_0 + \rho_e T^{1/2} - \rho_K \ln(T) + \rho_p T^5$$

, which encompasses the electron-electron ($e-e$) interaction that follows a $T^{1/2}$ dependence, the Kondo-like spin scattering with the $\ln T$ term, and the electron-phonon ($e-ph$) scattering that goes as T^5 . The fit to the data is presented in Fig.5, and the fitting parameters are given in Table.II. The magnitude of ρ_K is one order higher than ρ_e , indicating the dominance of Kondo-like scattering in these high Mn-content compositions. Our electronic structure calculations already point towards a scenario

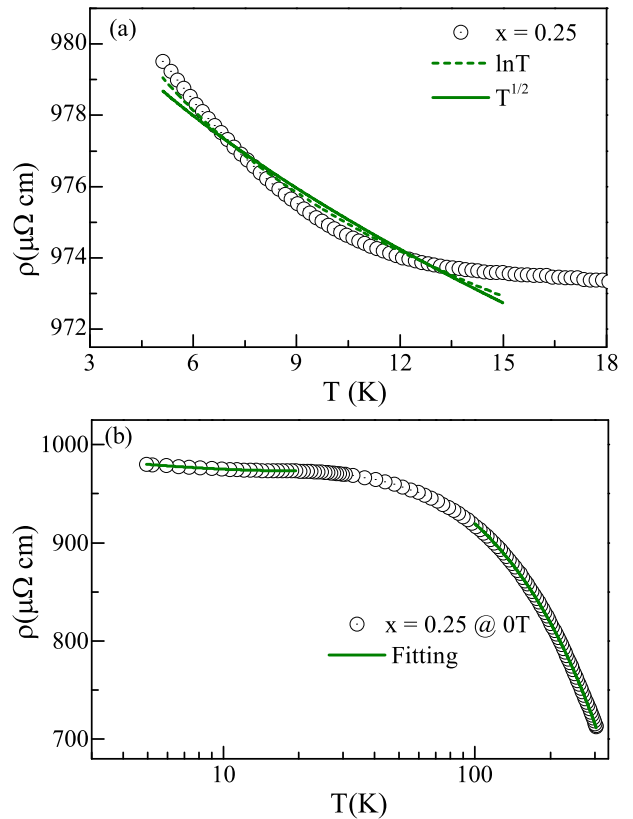


FIG. 5. (a) Fitting of temperature-dependent resistivity data of $x = 0.25$ at 0 T for individual contribution of the Kondo-like spin scattering and electron-electron interaction for $T \leq 20$ K, (b) and (c) shows the fitting of temperature-dependent resistivity data of $x = 0.25$ at 0 T and 5 T as per the equation given in the text.

where localized moments reside at the Mn-sites that interact through the cloud of conduction electrons formed by Fe and Ti atoms.

Alternatively, the magnetic field dependence of electrical resistance at fixed temperatures also presents the same scenario as that of $\rho(T)$. Fig.6 shows the isothermal magnetoresistance (MR) curves measured at different temperatures ranging from $5 \text{ K} \leq T \leq 300 \text{ K}$ and for all four compositions. Using the standard definition of MR as, $MR(\%) = \left[\frac{\rho(H) - \rho(0)}{\rho(0)} \right] \times 100$, we find that all the Mn-substituted compositions show the isotropic negative MR in the entire temperature range. Due to the dominance of electron-phonon scattering in the high-temperature regime, the MR curves exhibit linearity with changing magnetic fields. However, at low temperatures, a slight deviation from linearity is observed. Besides, in $x = 0.25, 0.3$, a sharp increase in the magnitude of the MR is observed at temperatures below 20 K, where the cusp-like feature was observed in $\rho(T)$. A power law fitting to the low-temperature MR data provides an exponent value of ~ 0.471 , which is as per the Altshuler-Aronov model

TABLE II. The extracted parameters after fitting the $\rho(T)$ data in low and high-temperature regions for the applied fields of 0 and 5T.

x	$\rho_0 \times 10^{-4}$		$\rho_e \times 10^{-6}$		$\rho_K \times 10^{-5}$		$\rho_p \times 10^{-14}$		$\rho_{ep} \times 10^{-7}$	$\rho_{em} \times 10^{-11}$
	0T	5T	0T	5T	0T	5T	0T	5T		
0.25	9.905	9.171	8.083	10.747	1.786	1.388	6.554	19.91	9.95	5.42
0.30	10.6	9.965	4.029	8.318	1.372	1.346	84.906	24.386	1.179	25.33

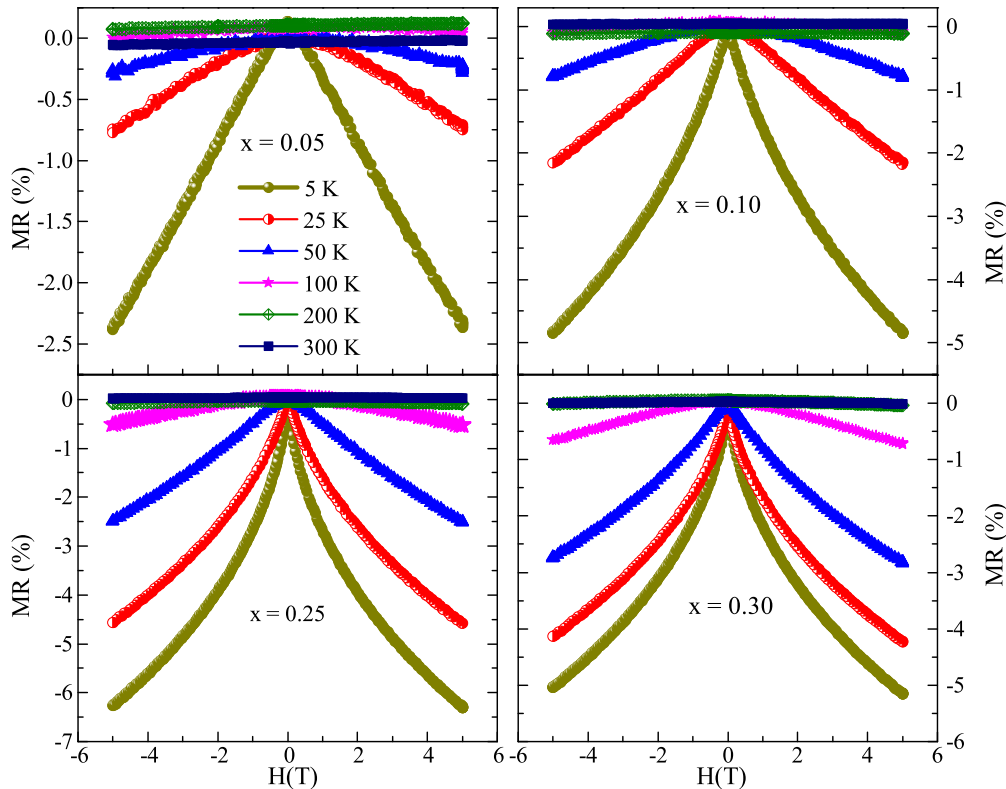


FIG. 6. Field dependent magnetoresistance of $\text{Fe}_2\text{Ti}_{1-x}\text{Mn}_x\text{Sn}$.

that predicts an electron-electron correlation dominated MR to have a $H^{1/2}$ dependence[32].

Having understood the electronic DOS in the $\text{Fe}_2\text{Ti}_{1-x}\text{Mn}_x\text{Sn}$ compositions and half-metallic ground state in $x \geq 0.25$, we now discuss the experimental study of its magnetic properties. The temperature-dependent magnetization, $M(T)$, plotted in Fig.7. According to the previous studies, an inherent Fe/Ti antisite disorder in the otherwise non-magnetic Fe_2TiSn induces the formation of weak magnetic clusters[33]. These interactions are identified by a step-like feature in the high-temperature region, denoted here as T_S , in the $M(T)$ curve. This step-like feature shifts towards the high-temperature side with rising Mn substitution. Additionally, at low-temperatures an abrupt rise in magnetization is observed marking the transition to a magnetically ordered state. This temperature is identified as T_C and its value increases with rising Mn content. The value of T_C

and T_S are listed in Table.I.

For small values of applied magnetic field, there is a noticeable contrast between the $M(T)$ plots recorded during the zero field cooled (ZFC) and field cooled (FC) protocols. This bifurcation between ZFC/ FC disappears when a relatively strong magnetic field of ≥ 0.1 T is applied (Fig.8), indicating the presence of weak anisotropy in the material. In the ZFC process, the material's anisotropy determines the amount of magnetization below T_C and may prevent a relatively small applied field from aligning the moments in the direction of the field. When the same material is cooled through T_C while being exposed to a magnetic field during the FC process, the moments are locked into the direction of the applied magnetic field. As a result, for small applied fields, there is a noticeable contrast between the ZFC and FC curves, and this bifurcation disappears when a slightly stronger magnetic field is applied.

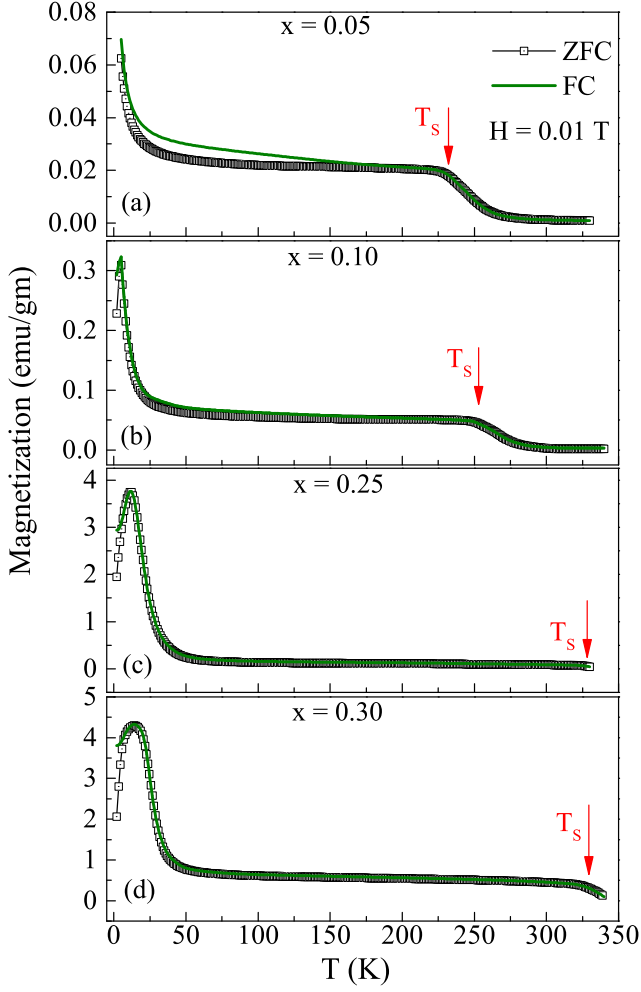


FIG. 7. Temperature dependence of the magnetization, $M(T)$ curves, of (a) $x = 0.05$, (b) $x = 0.10$, (c) $x = 0.25$, and (d) $x = 0.30$.

As seen from the electronic structure calculations, the substitution of Mn in Fe_2TiSn enhances the magnetic properties by introducing strong local moments at Mn sites. Accordingly, the isothermal magnetization $M(H)$ of all the Mn-compositions measured at 5 K shows a sizable increase in the magnetic moment values at a small applied field (see Fig.9(a)). The magnetic moment per formula unit extracted from extrapolating the near saturation $M(H)$ data, is found to exactly follow the Slater-Pauling rule (see Fig. 9(b)), reflecting the half-metallic state nature of $\text{Fe}_2\text{Ti}_{1-x}\text{Mn}_x\text{Sn}$ compositions. However, it may be noted that the $M(H)$ curves do not reach complete saturation, nor yield a good fit to the usual modified Langevin function, $M(H) = M_s L(\alpha) + \chi H$, where $\alpha = \mu H/k_B T$, M_s represent the saturation magnetization, μ is the average magnetic moment and χ represents the paramagnetic susceptibility. Thus ruling out any magnetic cluster-like evolution in the prepared compositions.

Alternatively, from the measurements, it appears that the Mn-substituted Fe_2TiSn compositions display a long-

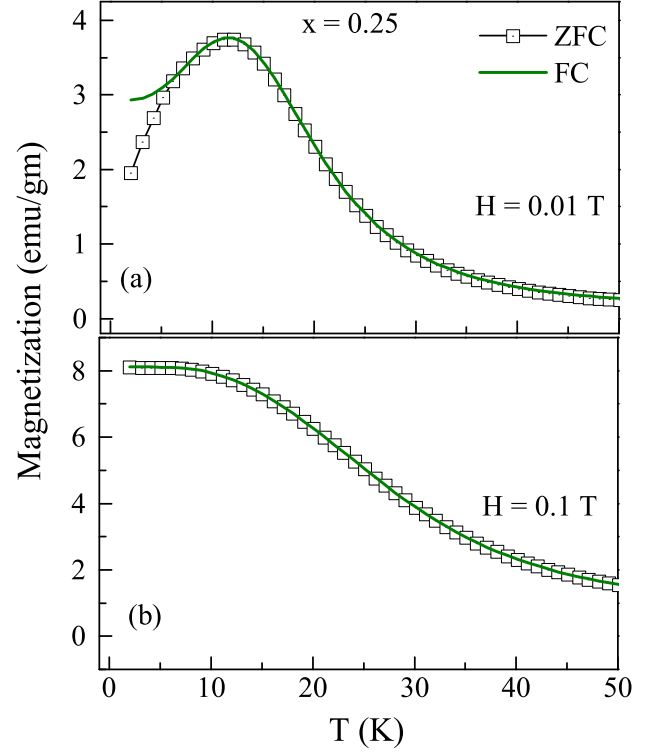


FIG. 8. Temperature dependence of the magnetization, $M(T)$ curves, of $x = 0.25$ at an applied magnetic field of (a) $H = 0.01$ T, and (b) $H = 0.1$ T.

range ferromagnetic order below T_C , which exhibits a substantial dependency on the strength of the applied magnetic field with respect to the random anisotropy. Further, the $\rho(T)$ data shows the Kondo-like behavior i.e. the presence of local Mn moment screened by conduction electrons, a weak random anisotropy model[34] could be applicable here. Such a model has previously been extensively used to explain the short-range FM correlations in Huesler alloys[35–37]. This model incorporates both the experimentally applied magnetic field and the ground state configuration of magnetic materials with random anisotropy for a wide range of anisotropy strengths. Three distinct regimes can be identified for the weak anisotropy situation based on the magnitude of the applied magnetic field, H , and the parameter H_S ($= H_r^4/H_{ex}^3$), where H_r and H_{ex} are anisotropic and exchange fields, respectively. For $H < H_S$, one obtains a correlated spin glass phase with a high magnetic susceptibility for low fields. When $H_S < H < H_{ex}$, a ferromagnet with a wandering axis (FMWA) results from a rough alignment of the spins in the presence of a weak magnetic field. The tipping angle of the magnetization vector with respect to the applied field changes throughout the system due to the non-collinear magnetic structure. In this

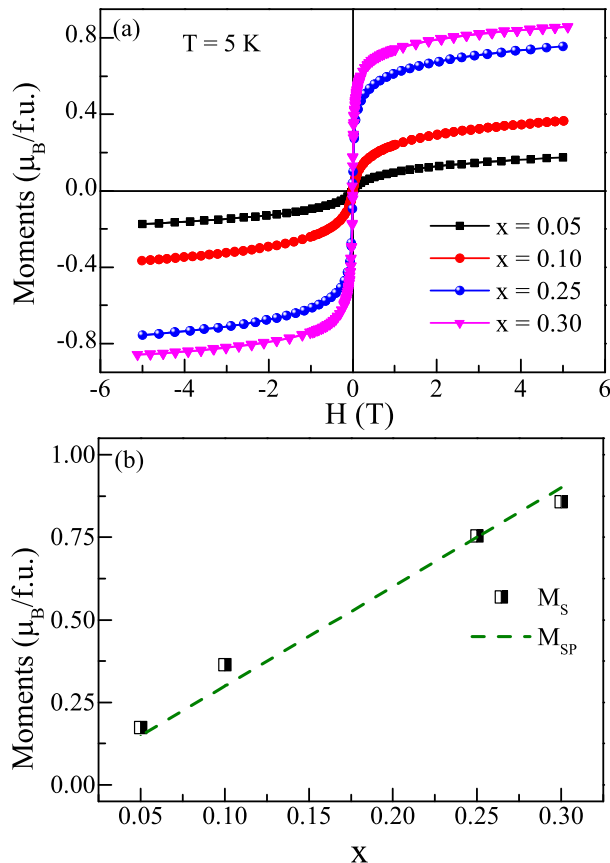


FIG. 9. (a) Isothermal magnetization, $M(H)$ curve measured at 5 K and (b) values of experimental saturation magnetization (M_S) at 5 K are plotted along with the Slater-Pauling empirical rule (dotted line) for varying Mn concentration.

regime, the magnetization approaches saturation as,

$$M(H) = M_s \left[1 - \frac{1}{15} \left(\frac{H_s}{H + H_c} \right)^{\frac{1}{2}} \right] \quad (1)$$

where M_s is saturation magnetization, and H_c is the field due to the coherent portion of the anisotropy. In the third regime where $H \gg H_s$, the correlation length of the spins reduces as the field strength increases, whereas the tipping angle is completely uncorrelated amongst sites. Except for a slight tipping angle (less than in the case of FMWA) brought on by random anisotropy, all spins in this regime are almost aligned with the field. In such cases, isothermal magnetization gradually approaches saturation as,

$$M(H) = M_s \left[1 - \frac{1}{15} \left(\frac{H_r}{H + H_{ex}} \right)^2 \right] \quad (2)$$

We have fitted equation(1) with an additional paramagnetic contribution, χH [38], to the $M(H)$ curve at 5 K for $x = 0.25$, as shown in Fig.10. It shows a satisfactory fit

for a wide range of applied fields from 0.4 to 5 T. The value of H_s derived after the fitting ranges from 0.303 T for $x = 0.05$ to 0.021 T for $x = 0.30$, which is lower than the maximum applied field, following the condition for the system to fall in the second regime. In contrast, the fitting of equation(2) does not yield a good fit to the data (see the dashed line in Fig.10 and the value of H_s derived after the fitting is much higher than the maximum applied field despite using the prefactor equal to 1 instead of $1/15$ [36].

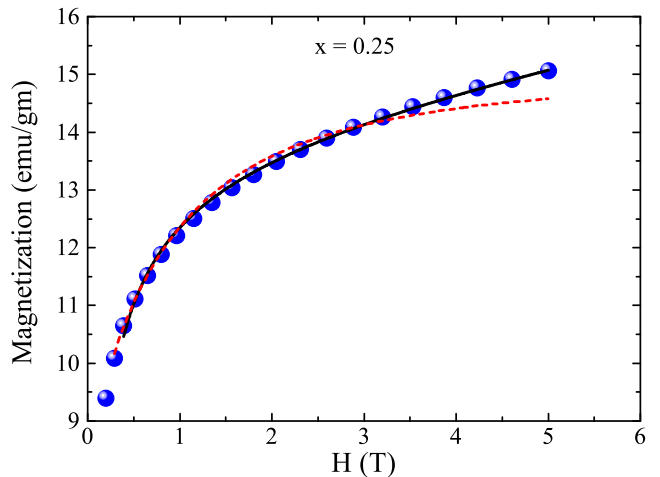


FIG. 10. M-H plot of the samples at 5K along with fit for, (a) $x = 0.25$. The dashed line shows the fitting of eq. (2) with prefactor equal to unity, and the solid black line represents the fitting of eq. (1) with adding paramagnetic contribution, χH .

Thus, the analysis of ab initio DOS calculation, resistivity, and magnetic data suggests that Mn substitution in Fe_2TiSn introduces localized moments. These local moments exhibit strong coupling with the conduction electron, which screens the interaction between two Mn atoms. As the results of this screening, the strength of the magnetic interaction decreases with increasing Mn-Mn distance, and typical ferromagnetic order is absent in $\text{Fe}_2\text{Ti}_{1-x}\text{Mn}_x\text{Sn}$. To verify this, we have calculated the distance-dependent magnetic exchange interaction (J_{Mn-Mn}) between two Mn atoms. Estimation of distance-dependent Mn-Mn magnetic interaction with smaller unit cells (considered for 25% substitution) is a difficult task. This is because, at large Mn-Mn separation in a small unit cell, contributions from the periodic images of Mn atoms at relatively shorter distances will start contributing to the magnetic energy. To avoid this problem, one has to consider a large supercell. We consider a $2 \times 2 \times 2$ supercell and replace two Ti with Mn atoms. The distance-dependent Mn-Mn magnetic interaction ($J_{Mn-Mn} = E_{AFM} - E_{FM}$) is then estimated as explained in the "Experimental and Computational details" section. Here, we take advantage of the fact that the magnetic moments on Fe and Ti atoms are negligibly small, and hence their insignificant direct contributions

to J_{Mn-Mn} can safely be ignored. The plot of separation dependent J_{Mn-Mn} is shown in Fig. 11. One can observe that the effective Mn-Mn interaction is ferromagnetic, consistent with the experimental findings. This ferromagnetic interaction exponentially decreases with the Mn-Mn separation and nearly zeroed at the separation of 8.51Å.

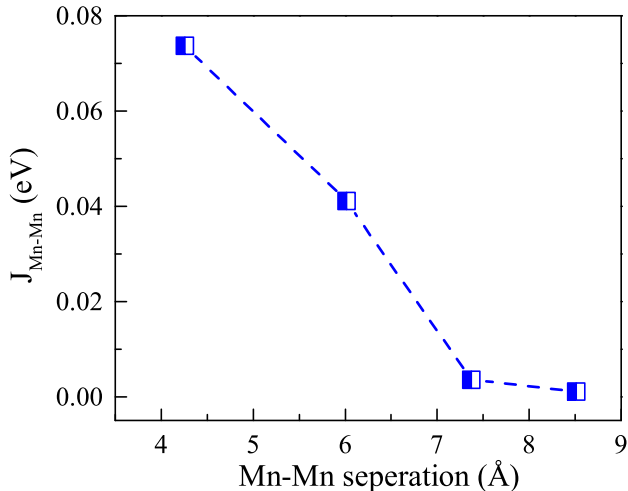


FIG. 11. Mn-Mn magnetic interaction at various separations in the unit cell is estimated by the total energy difference between antiferromagnetic and ferromagnetic states. For details refer to the Methods section.

Hence, according to the results of magnetic measurements, the magnetic state of $Fe_2Ti_{1-x}Mn_xSn$ changes with temperature as marked in the x - T phase diagram, as shown in the Fig.12(a). $Fe_2Ti_{1-x}Mn_xSn$ is in a typical PM state when the temperature is higher than T_s . As temperature decreases ferromagnetic correlation appears due to the formation of magnetic clusters. In the case of $x < x_c$ (region-I), clusters continue to evolve with falling temperatures and lead to a superparamagnetic ground state. No long-range magnetic order is observed in this region. The simplified schematic diagram of the magnetic state as a function of temperature is presented in Fig.12(b). Substituting higher Mn content ($x > x_c$) in place of Ti in $Fe_2Ti_{1-x}Mn_xSn$ significantly alters this magnetic behavior. The strong local moments of Mn suppress the influence of high-temperature FM clusters on the low-temperature magnetic ground state and result in an unconventional ferromagnetic ordering driven by random anisotropy, known as the "ferromagnet with wandering axis" state, as represented as region-II in the phase diagram. This transition from a superparamagnetic state in Fe_2TiSn to a weak random anisotropy-driven state with Mn substitution underscores the significant impact of Mn substitution on the magnetic properties of Heusler alloys. Furthermore, as confirmed from DFT calculation, electrical resistivity, and magnetic measurements, Mn substitution induces half-metallicity in the $Fe_2Ti_{1-x}Mn_xSn$, enhancing its potential for spin-

tronic applications.

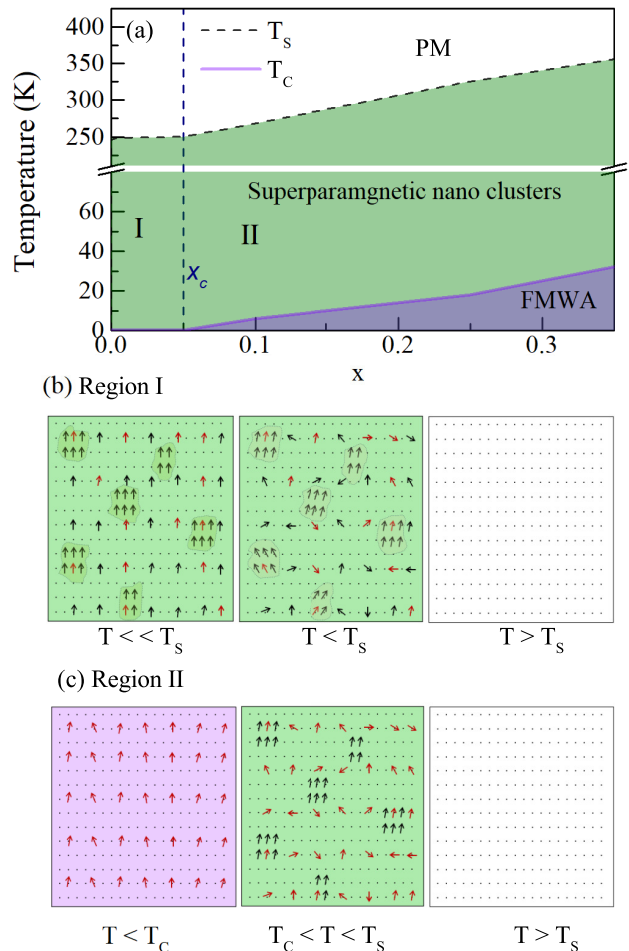


FIG. 12. x - T phase diagram representing the change in the magnetic state of $Fe_2Ti_{1-x}Mn_xSn$ with the decrease in the temperature. The local Mn moments (red arrow) align at an angle with the direction of the applied magnetic field.

IV. CONCLUSION

In this study, structural, magnetic, and transport properties of Mn substituted Fe_2TiSn have been investigated through room temperature XRD, temperature and field-dependent magnetization, and magnetotransport measurements. The room temperature powder X-ray diffraction patterns of all the $Fe_2Ti_{1-x}Mn_xSn$ compositions are indexed to $Fm\bar{3}m$ symmetry with an ordered $L2_1$ crystal structure. The lattice constants decrease systematically with rising Mn content. The temperature variation of electrical resistivity $Fe_2Ti_{1-x}Mn_xSn$ shows an overall increase in the magnitude with increasing Mn content. For $x \geq 0.25$, $\rho(T)$ shows a negative temperature coefficient of resistance, followed by an upturn at $T < 20$ K. The low-temperature upturn is due to

the combined effect of electron-electron correlation and strong Kondo-like spin scattering. The $\rho(T)$ above 100 K is dominated by the electron-phonon scattering, with a small contribution from the electron-magnon scattering as well, which indicates the presence of spin-polarized density of state in these compositions. Electrical transport along with the density of states calculation confirms the formation of highly spin-polarized electronic structures and the presence of half-metallicity on Mn substituted Fe_2TiSn .

Magnetization recorded as a function of temperature exhibits signatures akin to magnetic ordering and shifts to higher temperatures with increasing Mn concentration. Such a trend indicates the presence of a strong local magnetic moment of Mn atoms. However, the same $M(T)$ curves, upon application of magnetic fields of higher magnitude display features that hint towards the presence of anisotropy in the system. Besides, a step-like feature is recorded at $T \geq 250$ K in all the $M(T)$ curves. Field-dependent magnetization, $M(H)$, recorded at fixed temperatures shows the presence of ferromagnetic correla-

tions even at 300 K. The low-temperature $M(H)$ suits a random anisotropy model suggesting that a ferromagnet with a wandering axis can be an apt description of the magnetic ground state of the $\text{Fe}_2\text{Ti}_{1-x}\text{Mn}_x\text{Sn}$ compositions.

V. ACKNOWLEDGEMENT

K.M. acknowledges DST-INSPIRE (File: DST/INSPIRE/03/2021/001384/IF190777), New Delhi, for providing the research fellowship. KM and PB thank Dr. Mukul Gupta, UGC-DAE CSR, Indore, for extending the X-ray diffraction facility. Acknowledgment is also due to Prof. J. G. Lin, Center for Condensed Matter Science, National Taiwan University, Taipei, Taiwan, for providing access to the magnetic measurement facility. We also thank Prof. Pratap Raychaudhuri and Ganesh Jangam for their help in magnetic measurement at the Tata Institute of Fundamental Research, Mumbai.

-
- [1] F. Heusler, *Verh. Dtsch. Phys. Ges.* **5** (1903).
 - [2] T. Krenke, E. Duman, M. Acet, E. F. Wassermann, X. Moya, and L. Mañosa, *Nat. Mater.* **4** (2005).
 - [3] P. A. Bhoje, K. R. Priolkar, and A. K. Nigam, *Applied Physics Letters* **91** (2007).
 - [4] S. J. Hashemifar, P. Kratzer, and M. Scheffler, *Phys. Rev. Lett.* **5** (2005).
 - [5] M. e. a. Jourdan, *Nat. Commun.* **94** (2014).
 - [6] C. L. Seaman, N. R. Dilley, M. C. de Andrade, J. Herrmann, M. B. Maple, and Z. Fisk, *Phys. Rev. B* **53** (1996).
 - [7] I. Galanakis, P. H. Dederichs, and N. Papanikolaou, *Phys. Rev. B* **66** (2002).
 - [8] E. Alleno, *Metals* **8** (2018).
 - [9] A. Ślebarski and J. Goraus, *Phys. Rev. B* **80** (2009).
 - [10] C. S. Lue, J. H. Ross, C. F. Chang, and H. D. Yang, *Phys. Rev. B* **60** (1999).
 - [11] C. S. Lue, J. H. R. Jr, K. D. D. Rathnayaka, D. G. Nangle, S. Y. Wu, and W.-H. Li, *J. Condens. Matter Phys.* **13** (2001).
 - [12] M. Vasundhara, V. Srinivas, and V. V. Rao, *Phys. Rev. B* **77** (2008).
 - [13] N. Reumann, A. Riss, F. Garmroudi, M. Parzer, J. Kovacevic, T. Mori, and E. Bauer, *Phys. Rev. B* **106** (2022).
 - [14] A. Ślebarski, M. B. Maple, E. J. Freeman, C. Sirvent, D. Tworuzska, M. Orzechowska, A. Wrona, A. Jezierski, S. Chiuzbaian, and M. Neumann, *Phys. Rev. B* **62** (2000).
 - [15] A. Ślebarski, M. B. Maple, A. Wrona, and A. Winiarska, *Phys. Rev. B* **63** (2001).
 - [16] M. Häfner, J. K. Viljas, D. Frustaglia, F. Pauly, M. Dreher, P. Nielaba, and J. C. Cuevas, *Phys. Rev. B* **77** (2008).
 - [17] S. Chaudhuri, P. A. Bhoje, and A. K. Nigam, *J. Phys. Condens. Matter* **30** (2017).
 - [18] S. Chaudhuri, D. Salas, V. Srihari, E. Welter, I. Karaman, and P. A. Bhoje, *Sci. Rep.* **11** (2021).
 - [19] P. Giannozzi, O. Andreussi, T. Brumme, O. Bunau, M. B. Nardelli, M. Calandra, R. Car, C. Cavazzoni, D. Ceresoli, M. Cococcioni, N. Colonna, I. Carnimeo, A. D. Corso, S. de Gironcoli, P. Delugas, R. A. DiStasio, A. Ferretti, A. Floris, G. Fratesi, G. Fugallo, R. Gebauer, U. Gerstmann, F. Giustino, T. Gorni, J. Jia, M. Kawamura, H.-Y. Ko, A. Kokalj, E. Küçükbenli, M. Lazzeri, M. Marsili, N. Marzari, F. Mauri, N. L. Nguyen, H.-V. Nguyen, A. O. de-la Roza, L. Paulatto, S. Poncé, D. Rocca, R. Sabatini, B. Santra, M. Schlipf, A. P. Seitsonen, A. Smogunov, I. Timrov, T. Thonhauser, P. Umari, N. Vast, X. Wu, and S. Baroni, *J. Phys. Condens. Matter* **29** (2017).
 - [20] P. Giannozzi, S. Baroni, N. Bonini, M. Calandra, R. Car, C. Cavazzoni, D. Ceresoli, G. L. Chiarotti, M. Cococcioni, I. Dabo, and et al., *J. Phys. Condens. Matter* **21** (2009).
 - [21] D. Vanderbilt, *Phys. Rev. B* **41** (1990).
 - [22] J. P. Perdew, K. Burke, and M. Ernzerhof, *Phys. Rev. Lett.* **77** (1996).
 - [23] J. Rodríguez-Carvajal, *Phys. B: Condens. Matter* **192** (1993).
 - [24] A. R. Denton and N. W. Ashcroft, *Phys. Rev. A* **43** (1991).
 - [25] J. S. Moodera and D. M. Mootoo, *Journal of Applied Physics* **76** (1994).
 - [26] S. Ouardi, G. H. Fecher, C. Felser, and J. Kubler, *Phys. Rev. Lett.* **110** (2013).
 - [27] J. Pierre and I. Karla, *J. Magn. Magn. Mater.* **217** (2000).
 - [28] L. Bainsla, A. I. Mallick, M. M. Raja, A. A. Coelho, A. K. Nigam, D. D. Johnson, A. Alam, and K. G. Suresh, *Phys. Rev. B* **92** (2015).
 - [29] Y. Venkateswara, S. Gupta, S. S. Samatham, M. R. Varma, Enamullah, K. G. Suresh, and A. Alam, *Phys.*

- Rev. B **97** (2018).
- [30] D. Gnida, K. Ciesielski, and D. Kaczorowski, Phys. Rev. B **103** (2021).
- [31] A. Ślebarski, J. Phys. D Appl. Phys. **39** (2006).
- [32] P. A. Lee and T. V. Ramakrishnan, Rev. Mod. Phys. **57** (1985).
- [33] S. Chaudhuri, P. A. Bhowe, A. Bhattacharya, and A. K. Nigam, J. Phys. Condens. Matter **31** (2018).
- [34] E. M. Chudnovsky, W. M. Saslow, and R. A. Serota, Phys. Rev. B **33** (1986).
- [35] R. Saha, V. Srinivas, and T. V. C. Rao, Phys. Rev. B **79** (2009).
- [36] M. Vasundhara, V. Srinivas, and V. V. Rao, Phys. Rev. B **78** (2008).
- [37] S. Mondal, C. Mazumdar, R. Ranganathan, E. Alleno, P. C. Sreeparvathy, V. Kanchana, and G. Vaitheeswaran, Phys. Rev. B **98** (2018).
- [38] P. M. Gehring, M. B. Salamon, A. del Moral, and J. I. Arnaudás, Phys. Rev. B **41** (1990).